25th ABCM International Congress of Mechanical Engineering
October 20-25, 2019, Uberlândia, MG, Brazil

COB-2019-1123
A STUDY OF STATIC AEROELASTIC EFFECTS ON WING CONFIGURATIONS IN TRANSONIC FLOWS

J Allan A. Lyrio
Instituto Tecnológico de Aeronáutica, ITA/CTE-E, São José dos Campos, SP, Brazil
j.allanantunes@gmail.com

João Luiz F. Azevedo
Instituto de Aeronáutica e Espaço, DCTA/IAE/ALA, São José dos Campos, SP, Brazil
joaoluiz.azevedo@gmail.com

Domingos A. Rade
Instituto Tecnológico de Aeronáutica, ITA/IEM-P, São José dos Campos, SP, Brazil
rade@ita.br

Ricardo G. da Silva
Instituto de Aeronáutica e Espaço, DCTA/IAE/ALA, São José dos Campos, SP, Brazil
ri_galdino@yahoo.com.br

Abstract. *Transonic flows at high Reynolds numbers can lead to high dynamic pressures and, consequently, aerostructural deflections of the aircraft structures, mainly in the wings. As a consequence, Computational Fluid Dynamics (CFD) tools have been widely integrated with Computational Solid Mechanics (CSM) solvers based on finite element discretization in order to improve predictions of the aerodynamic performance and aircraft structural loads. The main objective of this paper is to describe the methodology and the numerical effort to integrate an in-house CFD code, named BRU3D, with a CSM solver for static aeroelastic applications in a high fidelity approach. The case used for the present validation effort is the static aeroelastic results from the HIRENASD project. Surface pressure distributions from BRU3D simulations are transferred to the structural model via shape functions, defined for the constant-stress triangular finite element, and deflections obtained from modulized static structural analysis are transferred to the CFD fluid mesh with the help of a Radial Basis Function (RBF) approach. All procedures have been implemented in FORTRAN and integrated via shell script, and results demonstrating converged wing surface pressures and deflections are compared to available experimental data.*

Keywords: *Computational Fluid Dynamics, Computational Structure Mechanics, Radial Basis Function, Static Aeroelasticity, Modal Basis.*

1. INTRODUCTION

According to Kroll *et al.* (2008), the aerodynamic performance of large transport aircraft operating at transonic speeds is highly influenced by wing deformation under aerodynamic loads. In last decades, many aeronautical research institutes, and also computer aided engineering companies, have invested in improving accuracy and efficiency of numerical and experimental fluid-structure interaction (FSI) analysis for both static and dynamic aeroelasticity. A remarkable example is the High Reynolds Number Aerostructural Dynamics (HIRENASD) project described by Ballmann *et al.* (2006), which was directed towards providing experimental wind tunnel data to improve the aero-structural dynamics understanding and knowledge in the transonic regime at Reynolds numbers typical of full scale transport aircraft.

The BRU3D CFD code has been widely used at Instituto de Aeronáutica e Espaço (IAE) for aerospace simulations at high Reynolds number and also at high Mach numbers. Recently, da Silva and Azevedo (2016) described the successful effort for BRU3D validation in pure aerodynamics problems using the ONERA-M6 and DLR-F6 configurations. The present work focuses in the description of the recent achievements with respect to the theoretical development and computational implementation of a fluid-structure interaction process using the BRU3D code loosely coupled to a modal-based CSM code.

An modal based structural module was developed in FORTRAN that is capable to use an NASTRAN (MSC, 2004) modal response result to calculate static structural deflections, reducing the finite element model to be used in each FSI iteration. This method is specially interesting due to the fact that it eliminates full CSM solver execution in each

aerostructural interaction and reduces the structural problem by normal mode basis truncation.

2. THEORETICAL AND NUMERICAL FORMULATION

2.1 Aerodynamic Modeling

The fluid dynamics formulation present in the BRU3D code is described by Junqueira-Junior *et al.* (2013). It is based on the 3-D compressible Reynolds-Averaged Navier-Stokes (RANS) equations, that filter the fluctuation part of the fluid, treated via turbulence models, and maintains only the mean contribution of the flow. These equations are also presented by da Silva and Azevedo (2016) in their dimensional form as:

$$\frac{\partial \mathbf{Q}}{\partial t} + \nabla.(\mathbf{E}_e - \mathbf{E}_v) = 0, \tag{1}$$

in which $\mathbf{Q}$ is given by

$$\mathbf{Q} = [\rho\ \rho u\ \rho v\ \rho w\ \rho\tau_1\ \rho\tau_2]^T, \tag{2}$$

and, $\mathbf{E}_e$ and $\mathbf{E}_v$ are, respectively, the inviscid and viscous flux vectors:

$$\mathbf{E}_e = \begin{bmatrix} \rho\mathbf{v} \\ (\rho u\mathbf{v} + p\hat{i}_x) \\ (\rho v\mathbf{v} + p\hat{i}_y) \\ (\rho w\mathbf{v} + p\hat{i}_z) \\ (e+p)\mathbf{v} \\ \tau_1\mathbf{v} \\ \tau_2\mathbf{v} \end{bmatrix}, \mathbf{E}_v = \begin{bmatrix} 0 \\ (\tau^l_{xi} + \tau^t_{xi})\hat{i}_i \\ (\tau^l_{yi} + \tau^t_{yi})\hat{i}_i \\ (\tau^l_{zi} + \tau^t_{zi})\hat{i}_i \\ (\beta^l_i + \beta^t_i)\hat{i}_i \\ \mu_{diff_1}\tau_{1,i}\hat{i}_i \\ \mu_{diff_2}\tau_{2,i}\hat{i}_i \end{bmatrix}, \tag{3}$$

with,

$$\beta_i = \tau_{ij}u_j - q_{Hi} \tag{4}$$

where ρ stands for the density, $\mathbf{v} = \{u, v, w\}$ is the velocity vector in Cartesian coordinates, p is the static pressure, $\tau_{\mathbf{ij}}$ is the viscous stress tensor, $\mathbf{q}_H$ is the heat flux vector, e is the total energy per unit volume. The $\hat{i}_x$, $\hat{i}_y$ and $\hat{i}_z$ terms are the Cartesian coordinate orthonormal vector basis. The dynamic viscosity from the shear stress tensor is determined by Sutherland's formula. According to Junqueira-Junior *et al.* (2013), the code solves equations in an unstructured, cell-centered, conservative finite-volume formulation and advective terms are computed using the 2nd-order Roe scheme.

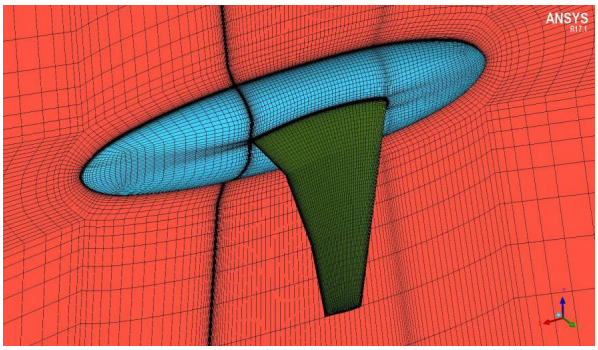

Figure 1: HIRENASD structured surface and symmetry grid in perspective view.

The numerical domain to be considered in the present work consists in a block-structured hexahedral volumetric grid with quadrilateral surface mesh as showed in Figure 1. Mesh data are provided in CFD General Notation System (CGNS) format version 2.4 with double precision by ANSYS Germany for the 1st AIAA Aeroelastic Prediction Workshop, AePW-1 (2012). These grids are refined enough to achieve the boundary layer discretization for $Y^+ = 1$ according to the Reynolds number range tested in the European Transonic Wind Tunnel (ETW), as presented in Table 1.

In order to perform morphing mesh capability tests for the first time, a coarse mesh was generated from Grid 1 of Table 1 by increasing the size of the first element off the wall and, hence, avoiding premature boundary layer mesh collapse during the FSI process. Table 2 contains information about the mesh used in the presented work where Y^+ become greater than one. The results from the approach used here are verified against available experimental data and they are discussed in next chapters.

Table 1: AePW provided HIRENASD meshes characteristics: non-dimensional wall distance, wing initial normal spacing ($Re = 23 \times 10^6$ based on $C_{ref} = 0.3445m$) and mesh size according AePW-1 (2012).

Mesh	Y+	First element	Mesh size
Grid 1	1	4.41×10^{-7}	3×10^6
Grid 2	2/3	2.94×10^{-7}	10×10^6
Grid 3	4/9	1.96×10^{-7}	28×10^6

Table 2: Coarse mesh generated from HIRENASD Grid 1 for the present study involving mesh deformation.

Mesh	Y+	First element	Mesh size
Grid 1a	15	2×10^{-5}	3×10^6

2.2 Structural Modeling

The system of equations that governs the linear dynamic structure response can be obtained through the Hamilton Principle which, according to Brandão (1996), states:

$$\int_{t_1}^{t_2} (\delta L + \delta W) dt = 0,\ L = T + V, \tag{5}$$

where the L is the Lagrangian, T and V are, respectively, the kinetic and strain energy, and δW is the virtual work of the nonconservative forces and moments. Associating the Hamilton Principle with the finite element discretization of the structural domain, the equations of motion are obtained in the form:

$$\mathbf{M}\ddot{\mathbf{U}}(t) + \mathbf{C}\dot{\mathbf{U}}(t) + \mathbf{K}\mathbf{U}(t) = \mathbf{R}(t), \tag{6}$$

where $\mathbf{M}$, $\mathbf{C}$ and $\mathbf{K}$ are respectively the mass, viscous damping and stiffness matrices. In addition, $\mathbf{R}(t)$ is the vector of external forces and moments applied in the degrees of freedom and $\ddot{\mathbf{U}}(t)$, $\dot{\mathbf{U}}(t)$, $\mathbf{U}(t)$ are, respectively, the acceleration, velocity, and displacement response vectors of the system. When dynamic effects are neglected, the equation 6 can be reduced to a static equilibrium equation of the form:

$$\mathbf{K}\mathbf{U} = \mathbf{R}. \tag{7}$$

In order to perform the modal basis approach, the Rayleigh-Ritz method considers an approximation of the solution as a linear combination of linearly independent basis vectors that satisfy the geometrical boundary conditions. So, the structural dynamics problem in the classical form can be solved by obtaining the eigenvalues (natural frequencies) and eigenvectors (natural vibration modes) of the dynamic problem, these later being used as basis vectors, as follows:

$$(\mathbf{K} - \omega_i^2 \mathbf{M})\phi_i = \mathbf{0}, \tag{8}$$

$$\mathbf{U} = \sum_{i=1}^{n} \boldsymbol{q_i \phi_i} = \boldsymbol{\Phi \mathbf{q}}, \tag{9}$$

where Φ is the modal matrix (formed column-wise by the system eigenvectors) and $\mathbf{q}$ is the vector of modal coordinates. Associating equations 7 and 9, and making use of the orthogonality properties of the eigenvectors, one obtains the following solution for the reduced problem:

$$\mathbf{q} = \boldsymbol{\Lambda^{-1} \Phi^T \mathbf{R}}, \tag{10}$$

where Λ is the diagonal matrix formed by the system eigenvalues. Therefore, the static structural problem becomes dependent of the natural frequencies and associated modal shapes, and the aerodynamic forces applied on the wing surfaces elements are projected in those modes.

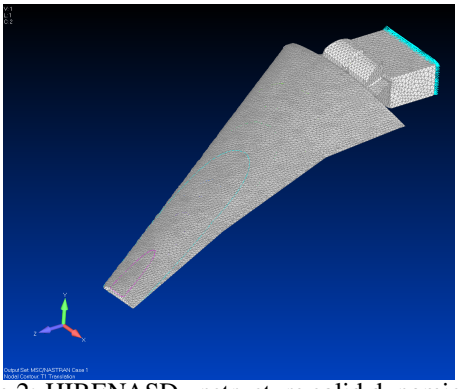

Figure 2: HIRENASD unstructure solid dynamic grid.

The numerical domain to be modulized consists in a FEM unstructured tetrahedral grid, showed in Figure 2 composed of wing, excitation transmission system and clamping flange for main balance connection. The NASTRAN format file model is available in AePW-1 (2012).

2.3 Load Transfer

According to Cebral and Lohner (1997), considerable differences in surface mesh discretization between fluid and solid domains, in loosely coupled approach for fluid-structure interaction problems, can lead to non-conservative load transfer. The approach using finite element shape functions, as showed by Farhat *et al.* (1998) and Chen (1999), is consistent, preserving force summation, and conservative, conserving virtual work, in the load transfer process. However, the results presented by de Boer *et al.* (2008) showed that conservative approaches could produce large oscillations in pressure fields, which increase as the flexibility of the structure is increased. Due to this fact and for simplicity of the computational implementation, the method developed in this paper considers only consistent load transfers.

In light of this, the aerodynamic loads generated in the BRU3D simulations, in terms of pressure distributions, must be transferred to finite element model degrees of freedom preserving the integral forces. Then, considering that the CFD code uses a finite volume method with constant pressure in the faces, an first step is to integrate force on each surface fluid element creating air loads vectors. In a second stage, the process finds the nearest structural element centroid and, then, uses the Constant Stress Triangle (CST) shape function formulation to distribute each CFD air loads to the finite element surface nodes. This method follows the so called "area coordinate approach" presented by Guruswamy (2002), and is illustrated in Fig. 3 where i, j and k are the structural nodes and gray dots are the surface fluid element centroids. Both implemented nearest element correlation procedure and sub-triangles areas calculations need to be performed only once in the beginning of process, saving time during the FSI calculations.

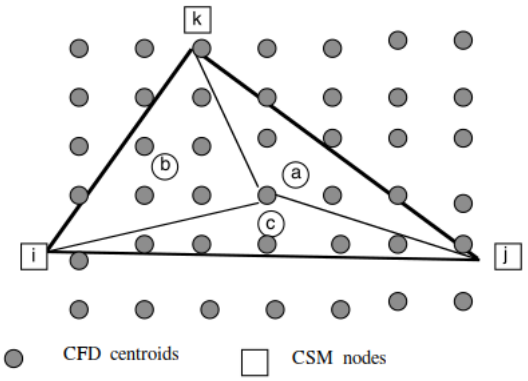

Figure 3: Interpolation based on triangular area coordinates (Guruswamy, 2002)

2.4 Fluid Mesh Morphing

Radial Basis Functions (RBF's) are widely used for multivariable interpolation. In this work, RBF numerical FORTRAN implementation for fluid mesh morphing is performed based on the work of Beckert and Wendland (2001), de Boer *et al.* (2006) and Rendall and Allen (2009). According de Boer *et al.* (2006), a node displacement calculated during

CSM analysis can be approximated by a sum of basis functions:

$$d_i(x) = \sum_{j=1}^{Nb} \alpha_j \phi(||x - x_{bj}||) + p(x) \tag{11}$$

where ϕ is a function based in Euclidean distance and p is a optional polynomial function for proper pure translation. In addition, α is the coefficient to be calculated to recover the displacement d_i, and N_b is the number of boundary points or the center of radial basis functions. In this work, the Wendland compactly supported functions are used, as prescribed by Beckert and Wendland (2001). Moreover, the system of equations for RBF calculation are performed in three directions ($\mathbf{d}_i(x) = [\Delta\mathbf{x}, \Delta\mathbf{y}, \Delta\mathbf{z}]$) for the calculation of the coefficients $\alpha_x, \alpha_y, \alpha_z$. Therefore, three linear systems of equations are solved iteractively using the GMRES method, Saad (2003). After this first stage of calculations, the volume mesh, indicated by subcript v, is updated using the **A** matrix:

$$\Delta\mathbf{x}_v = \mathbf{A}\alpha_x \tag{12}$$

where **A** is the dependence matrix from fluid nodes in respect to the prescribed RBF control points. The same procedure is performed for the y and z directions.

3. UNCOUPLED RESULTS

Before the process integration, the developed sub-processes for fluid mesh morphing, modulized structural static analysis and fluid solver were tested separately. Such results are presented in this chapter.

3.1 2D RBF Morphing Tests

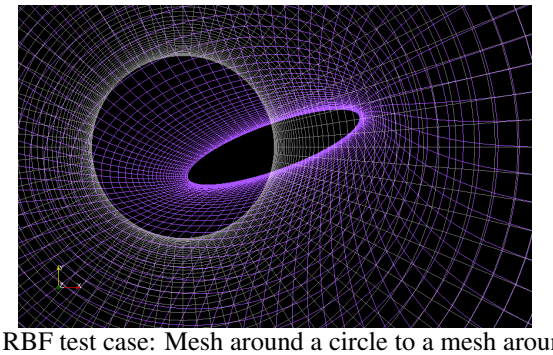

Figure 4: 2D RBF test case: Mesh around a circle to a mesh around an ellipse.

In order to first evaluate the ability of mesh deformation process, a parametric geometry and mesh were generated around an ellipse as illustrated in Figure 4. In such mesh it is possible to vary the initial and final ellipse radius ratio, the type of deformation to be made as well as mesh parameters, e.g., the first element near the wall and fair-field distance. In addition, two quality parameters are checked in the final mesh: presence of negative volumes and cell skewness according range criteria described in ANSYS (2015).

Given this, it is possible to check mesh quality in a efficient way for a simple mesh that has similar characteristics to a more complex mesh such as the HIRENASD mesh previously described. In the following test, the final mesh is evaluated for different ellipse rotation angle and radial basis function support radius values:

- Fixed geometric data:
  - Ellipse aspect ratio: 2.0
  - Translation (dx; dy): (0; 0)
- Geometric data variation:
  - Rotation angle: 5°, 10°,20° and 40°
- Fixed mesh parameters:
  - Mesh growth ratio: 1.1
  - First mesh element: 4×10^{-7}
  - Far Field radius: 10.0
  - Ellipse control points: 160
  - Farfield control points: 160
- Fixed RBF parameters:
  - function: Wendland C2
- RBF parameter variation:
  - Support radius: 1, 2, 4, 6 and 8

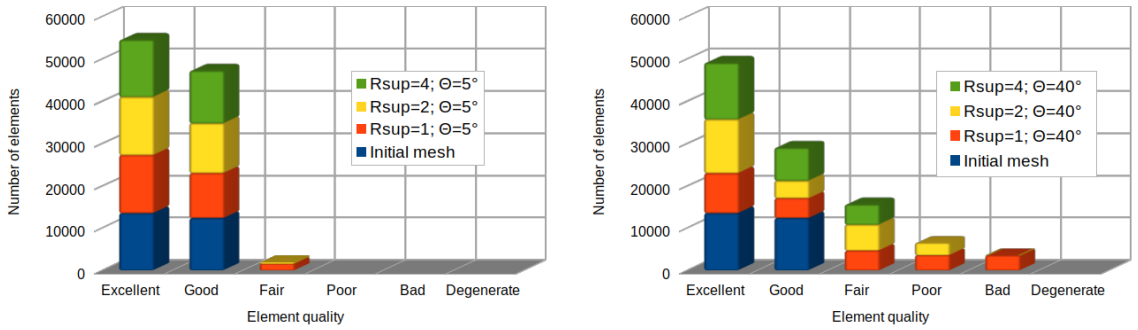

Figure 5: Mesh skewness as a function of support radius for ellipse rotation angle: 5 deg. (left) and 40 deg. (right)

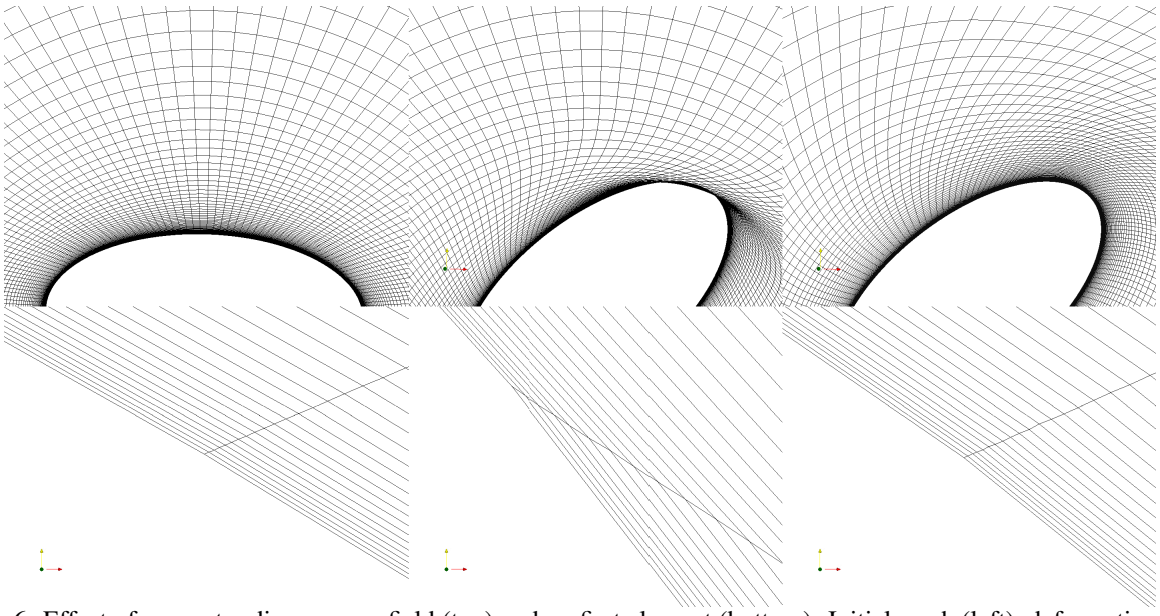

Figure 6: Effect of support radius on near field (top) and on first element (bottom): Initial mesh (left), deformation using $r_{sup} = 1$ (center) and $r_{sup} = 4$ (right).

Figure 5 shows 2D test mesh results in terms of skewness for minimum and maximum rotation angles. The initial mesh has only "excellent" and "good" elements. After $5°$ rotation, a few "fair" elements appear when $r_{sup} = 1$ *or* 2 are used. Furthermore, increasing the rotation angle to $40°$, "poor" and "bad" elements appear. The final mesh quality is considerable improved when $r_{sup} = 4$ is used.

For greater support radius, $r_{sup} = 6$ *and* 8, the linear system could not be solved and some investigation in the code shall be performed. However, according to de Boer *et al.* (2006), although quality and robustness can be increased by larger RBF support radii, such larger radii will reduce the sparsity of the linear system matrix and, hence, make the problem less efficient to be solved when using iterative methods.

A visual check of the support radius effect in the volumetric morphed mesh is presented in Fig. 6 where $r_{sup} = 1$ is generating $1{\times}10^3$ negative elements near to ellipse wall from total of $26{\times}10^3$ volume elements. When $r_{sup} = 4$ is used, no negative volumes are generated.

3.2 Modal Basis Verification

The Modal basis approach is used for structural deflection analysis instead of calling a FEM linear solver, e.g. NASTRAN, in each FSI iteration. In order to warrant enough structural representativeness, two studies are made: a) Wing tip displacement convergence analysis, and b) Eigenvalues comparisons between numerical and experimental results.

Figure 7 shows both HIRENASD wing tip leading (LE) and trailing (TE) edge z-displacement convergences for a given load versus the number considered of mode shapes, respectively blue and red curves. The dashed pointed black line and the dashed grey line represent the NASTRAN linear static results from MSC (2004). Comparing the modal and linear static results, it is possible to select the first 10 flexible mode shapes for FSI validation process. Moreover, the first five eigenfrequencies calculated using the FEM modal, presented in Figure 2, are compared against experimental and numerical result from Reimer *et al.* (2007). Table 3 shows such comparison. According Reimer *et al.* (2007), the

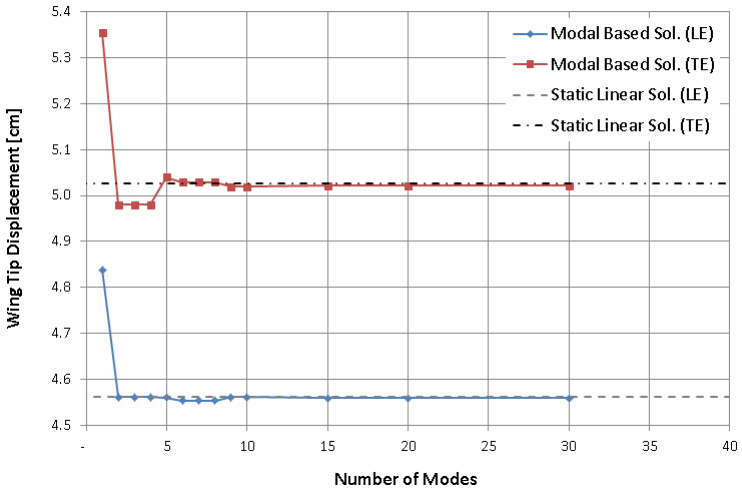

Figure 7: Displacement convergence analysis.

Table 3: Vacuum eigenfrequency [Hz] comparison: Present calculation versus experimental and calculated by Reimer *et al.* (2007).

Mode	Eigenshape	Present Work	Experimental	Reimer *et al.* (2007)
1	1st flap bending	26.7	25.8	26.6
2	2nd flap bending	86.4	71.75	87.2
3	1st slew bending	157.4	-	164.4
4	3rd flap bending	190.5	-	193.5
5	1st torsion	276.0	262.9	275.4

screw connections between clamping devices and main balance, not present in the modal used here, can reduce the model stiffness. For this reason the present calculated frequencies are quite higher than in the free vibration tests without wind. Despite the model differences, the calculated eigenfrequency set can be considered valid.

3.3 HIRENASD Selected Condition

Table 4 shows the HIRENASD wind tunnel test conditions selected to be simulated in the presented framework. Considering these cases, it is possible to investigate both pressure distribution and wing deflection results against experimental data available in AePW-1 (2012) and Ballmann *et al.* (2008).

Table 4: HIRENASD static aeroelastic condition to be simulated in the present work based on $C_{ref} = 0.3445\ m$ and $b_{ref} = 1.250\ m$, according to AePW-1 (2012).

ETW Series	Re	q/E$\times 10^6$	Mach	Angle of attack [deg]
1	7×10^6	0.22	0.80	0.5
1	7×10^6	0.22	0.80	1.5

3.4 Rigid Aerodynamic Simulation

A pure steady rigid BRU3D simulation is performed in the selected condition at $\alpha = 1.5$ in order to verify the capability of the solver to achieve convergence in such transonic flight condition as well as to obtained the "rigid shape" reference results for subsequent FSI simulation comparisons. Figure 8a shows both CL and CD convergence after one thousand CFD iterations and Figure 8b shows maximum residue from complete fluid domain convergence. The lift coefficient converges to 0.3429 and the drag to aproximately 0.0170.

The comparison between experimental pressure distributions from AePW-1 (2012) with BRU3D "rigid shape" simulation in several wing sections from Figure 9 is presented in Fig. 10. BRU3D rigid simulation results deviate from the experimental data in the wing upper surface on the outboard region mainly due to model deformation during the wind tunnel tests.

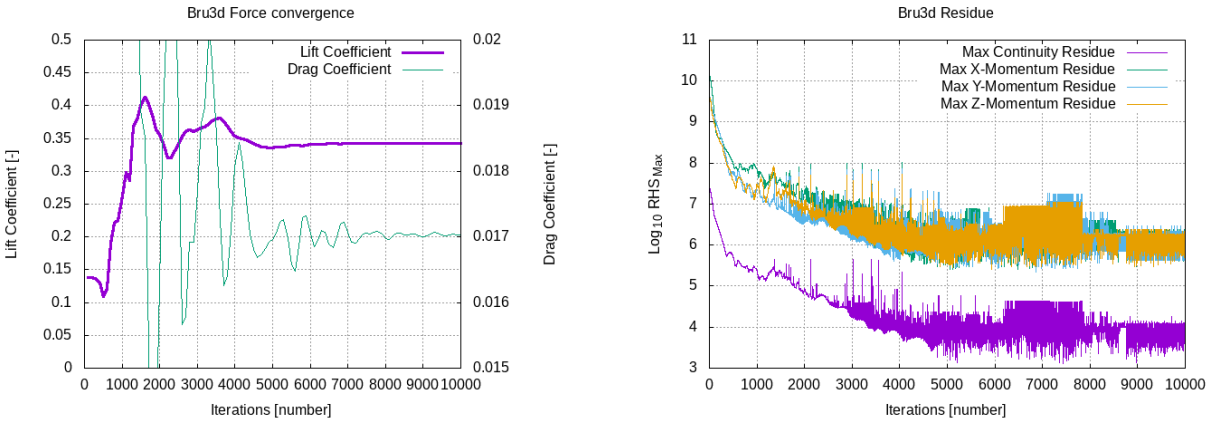

(a) Airloads convergence.

(b) Maximum residue history.

Figure 8: Aerodynamic coefficients and residue convergence for BRU3D at Mach=0.80, Re=7×10^6, AoA=1.5degs.

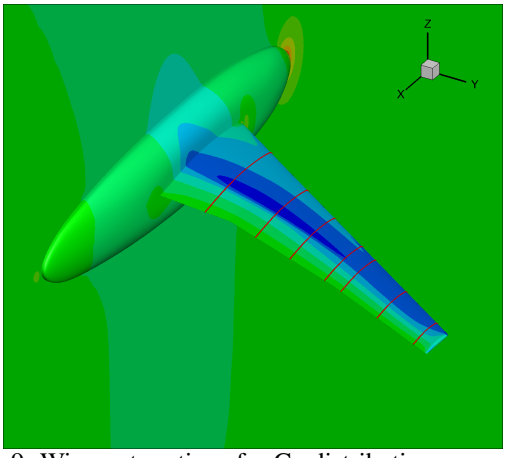

Figure 9: Wing cut sections for Cp distribution comparison.

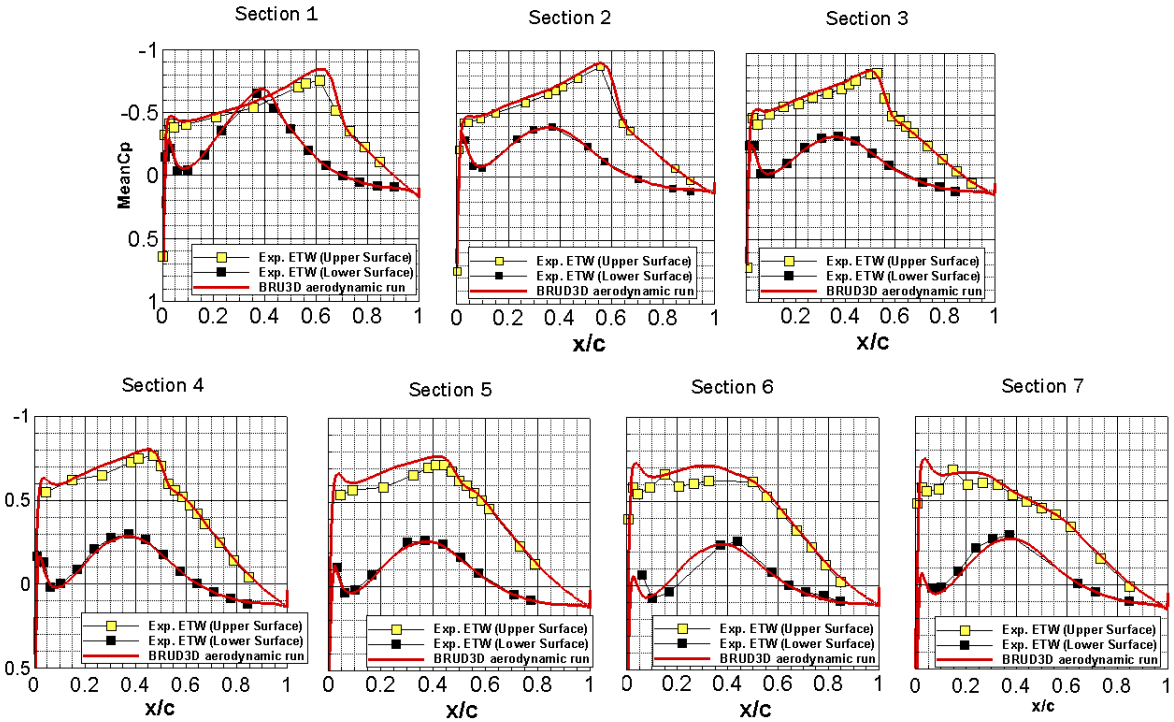

Figure 10: Comparison between BRU3D pure aerodynamic simulation versus HIRENASD Experiment from AePW-1 (2012) at Mach 0.80, q/E=0.22×10^{-6}, AoA=1.5degs.

4. COUPLED RESULTS

After all the sub-process tests, an integrated process for 3-D simulation was created in the UNIX environment where the FSI steps are represented by the four pre-compiled FORTRAN codes: BRU3D solver, LMT load mesh transfer, FEM modal-based code and RBF fluid mesh morphing.

4.1 FSI Process

Starting from the unloaded wing shape, the first CFD simulation is performed in the CeMEAI cluster (ICMC, 2019). The resulting wing pressure distribution is interpolated from CFD centroid surface elements to superficial CSM nodes (named here "transfer mesh") using the CST method previous discussed. Hence, the wing displacements are extract from FEM modal basis in the transfer mesh nodes and, then, provided to the RBF process imposing wing deflection for the fluid mesh motion. Here, it is important to mention that fuselage, symmetry and far field nodes are considered to have zero deflection during the RBF solution system and, consequently, for fluid mesh morphing. This process is repeated until aeroelastic equilibrium.

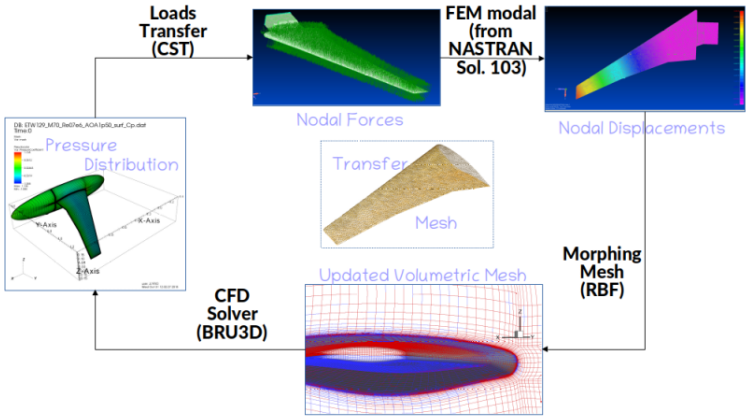

Figure 11: FSI sub-processes (represented by arrows) and input-output data (visualizations).

4.2 Steady Aeroelastic Simulation

When the BRU3D is coupled with the other FSI sub-processes, as previously presented, both aerodynamic results, by means of pressure distribution, and wing deformation, in terms of bending and twist, yield good agreement with the experimental data. Figure 12a shows convergence of both wing tip z-displacement and twist at $\alpha = 1.5$ after 10 iterations of the FSI process using a gradual load approach in order to avoid overshoots in the mesh morphing calculation. Moreover, Figure 12b plots the wing tip deflection for BRU3D coupled in the FSI process at $\alpha = 0.50$ and $\alpha = 1.5$ deg. and the experimental data from Chwalowski *et al.* (2011) for several angles of attack.

The use of a gradual transfer load transfer approach is implemented in the present study by increasing the loads by 20% in each FSI iteration until full application is reached. Such an approach is very robust, which is extremely important as the structure model becomes more flexible. Figure 13 shows the computed wing tip deflection after each RBF morphing execution. After aproximately six FSI iterations, the wing position converges to a loaded wing shape and the pressure distribution stops changing, as well as the integrated lift (CL), drag (CD), pitching moment (CMy) and rolling moment (CMx) coefficients. For a fixed angle of attack used here in this validation case, all aerodynamic coefficients converge as indicated in Table 5. The pressure distribution plots in Fig. 14 show comparisons between BRU3D rigid wing results, BRU3D results in the FSI coupled process and HIRENASD experiment data. The BRU3D results coupled in the FSI process yield a better match with the experimental data than the calculations with the rigid wing. Although the wing displacement and twist are small relative to the wing span, the impact in integrated aerodynamic coefficients is considerable and it cannot be neglected during either in the wind tunnel data analysis or for aircraft design.

5. FINAL REMARKS

The integration between BRU3D code and a modal-based static structural analysis code has been successfully implemented by the use of radial basis functions and shape functions for, respectively, fluid mesh deformation and pressure load transfer. The results obtained with this integrated FSI process is compared with the HIRENASD wind tunnel data in terms of pressure distributions and wing deflections, demonstrating agreement between computed and experimental results.

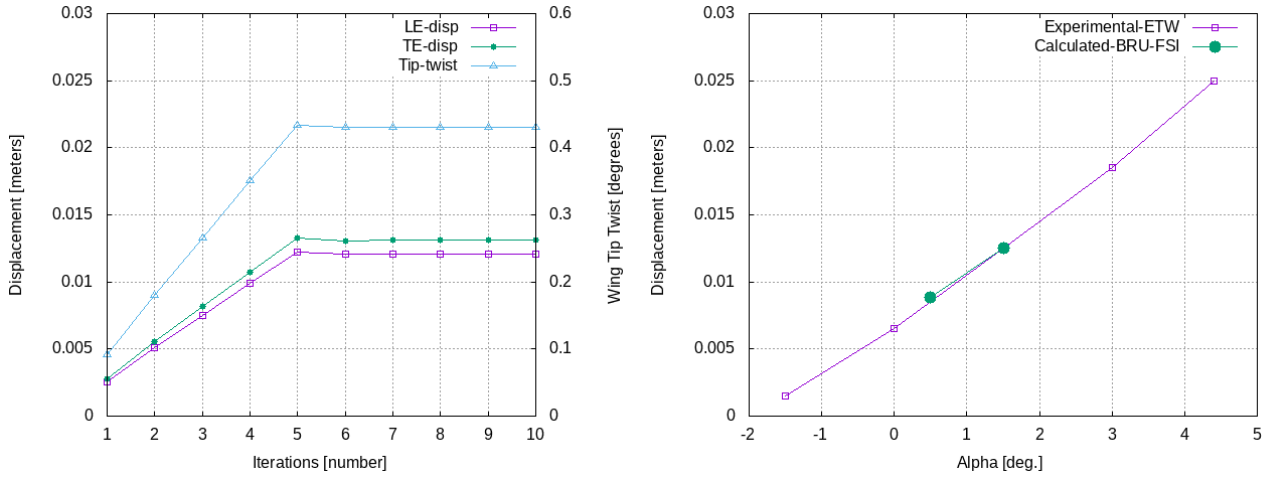

(a) Wing tip z-displacement and twist convergence at $\alpha = 1.5$ deg. (b) Wing tip z-displacement versus angle of attack.

Figure 12: BRU3D FSI run: Wing tip displacement and twist at Mach=0.80, Re=7×10^6, q/E=0.22×10^{-6}.

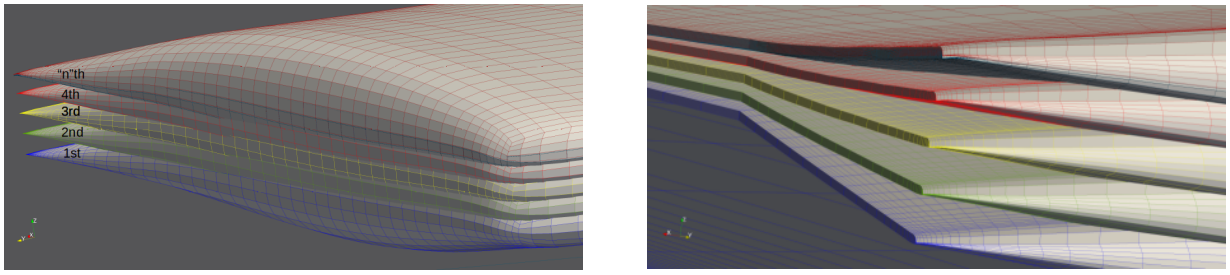

(a) Perspective view (b) Trailing edge detail.

Figure 13: BRU3D FSI run: Surface mesh deformation in the wing tip region during each iteration at Mach=0.80, Re=7×10^6, q/E=0.22×10^{-6}, AoA=1.5 deg.

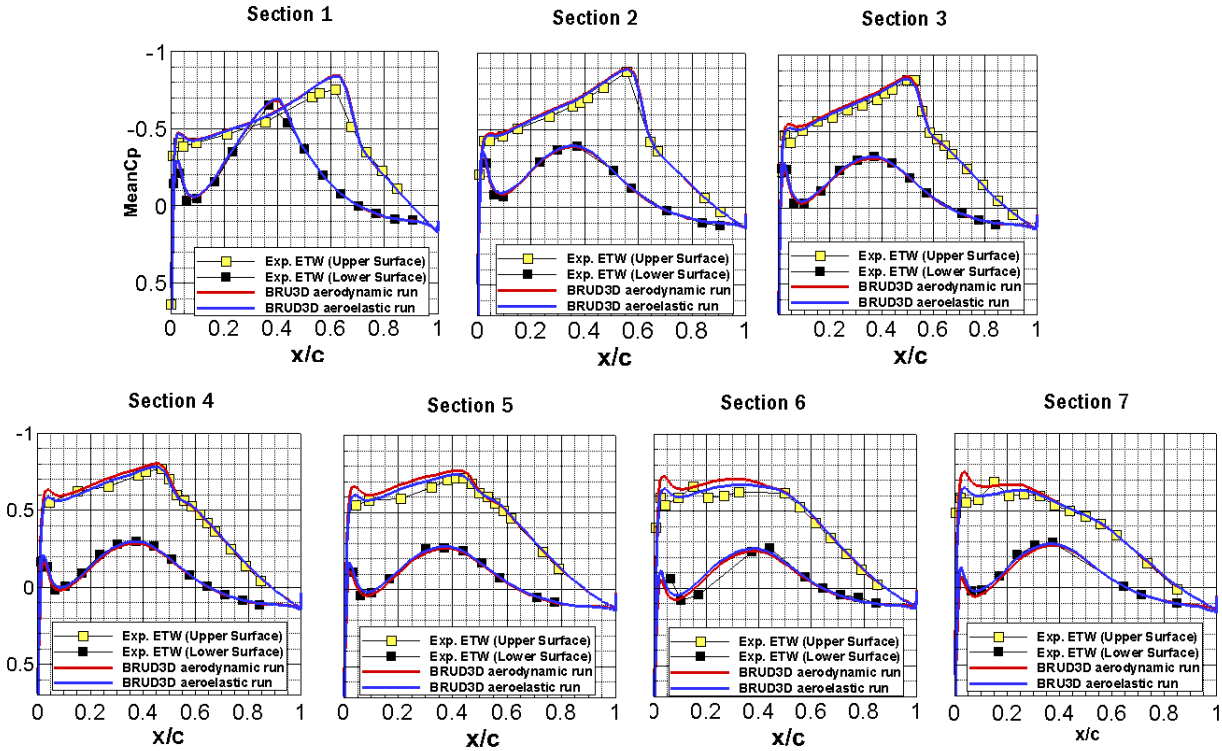

Figure 14: Comparison between BRU3D rigid wing, BRU3D in the FSI coupled process and HIRENASD Experiment at Mach=0.80, Re=7×10^6, q/E=0.22×10^{-6}, AoA=1.5 deg.

Table 5: BRU3D results with and without structural module coupled at Mach=0.80, Re=7×10^6, q/E=0.22×10^{-6}, AoA=1.5 deg.

Simulation	CL[-]	CD[-]	CMy[-]	CMx[-]
BRU3D Rigid	0.3429	0.0170	-0.2646	0.1030
BRU3D+Modal Coupled	0.3286	0.0165	-0.2518	0.0965
Variation	-4.14%	-2.94%	-4.84%	-6.35%

6. ACKNOWLEDGEMENTS

Research carried out using the computational resources of the Center for Mathematical Sciences Applied to Industry (CeMEAI) funded by FAPESP under Grant No. 2013/07375-0. The authors would like to thank Dr. Carlos Breviglieri Junior, for his help with the BRU3D code, and Mr. Rodrigo Marques, for his support in structural modeling issues. The authors further acknowledge the support for the present research provided by Conselho Nacional de Desenvolvimento Científico e Tecnológico, CNPq, under the Research Grants No. 309985/2013-7 and No. 402238/2013-3.

7. REFERENCES

AePW-1, 2012. "Aeroelastic Prediction Workshop". URL `https://c3.nasa.gov/dashlink/static/media/other/AEPW_legacy.htm`.

ANSYS, 2015. "Skewness Quality Measures". URL `https://www.sharcnet.ca/Software/Ansys/17.0/en-us/help/wb_msh/msh_skewness.html`.

Ballmann, J., Dafnis, A., Korsch, H., Buxel, C., Reimerdes, H.G., H, K., Oliver, H., Braun, C. and Barrs, A., 2008. "Experimental Analysis of High Reynolds Number Aero-Structural Dynamics in ETW". In *46th AIAA Aerospace Sciences Meeting and Exhibit*. Reno, NV, USA.

Ballmann, J., Dafnis, A., Braun, C., Korsch, H., Reimerdes, H.G. and Olivier, H., 2006. "The HIRENASD Project: High Reynolds Number Aerostructural Dynamics Experiments In The European Transonic Wind Tunnel ETW". In *25th International Congress of the Aeronautical Sciences*. Hamburg, Germany.

Beckert, A. and Wendland, H., 2001. "Multivariate interpolation for fluid-structure-interaction problems using radial basis functions". *Aerospace Science and Technology*, Vol. 5, No. 2, pp. 125–134.

Brandão, M.P., 1996. *Fundamentos da Dinâmica de Estruturas*. ITA, São José dos Campos, 1st edition.

Cebral, J.R. and Lohner, R., 1997. "Conservative load projection and tracking for fluid-structure problems". *AIAA Journal*, Vol. 35, No. 4, pp. 687–692.

Chen, S.P., 1999. "Implementation of Interaction Algorithm to Non-Matching Discrete Interfaces Between Structure and Fluid Mesh". Technical report, NASA Report.

Chwalowski, P., Florance, J.P., Heeg, J., Wieseman, C.D. and Perry, b.P., 2011. "Preliminary Computational Analysis of the HIRENASD Configuration in Preparation for the Aeroelastic Prediction Workshop". In *International Forum on Aeroelasticity and Structural Dynamics*. Paris, France.

da Silva, R.G. and Azevedo, J.L.F., 2016. "Numerical Simulations of Turbulent Flows Over the ONERA-M6 And DLR-F6 Configurations". In *30th Congress of the International Council of the Aeronautical Sciences*. Daejeon, Korea.

de Boer, A., van der Schoot, M.S. and Bijl, H., 2006. "New method for mesh moving based on radial basis function interpolation". In *European Conference on Computational Fluid Dynamics, ECCOMASS CFD*. TU Delft, NL.

de Boer, A., van Zuijlen, A.H. and Bijl, H., 2008. "Comparison of conservative and consistent approaches for the coupling of non-matching meshes". *Computer Methods in Applied Mechanics and Engineering*, Vol. 197, No. 49, pp. 4284–4297.

Farhat, C., Lesoinne, M. and Tallec, P.L., 1998. "Load and motion transfer algorithms for fluid-structure interaction problems with non-matching discrete interfaces: Momentum and energy conservation, optimal discretization and application to aeroelasticity". *Computer Methods in Applied Mechanics and Engineering*, Vol. 157, No. 1, pp. 95–114.

Guruswamy, G.P., 2002. "A review of numerical fluids/structures interface methods for computations using high-fidelity equations". *Computers and Structures*, Vol. 80, No. 1, pp. 31–41.

ICMC, 2019. "Centro de Ciências Matemáticas Aplicadas à Indústria". URL `http://www.cemeai.icmc.usp.br/`.

Junqueira-Junior, C., Azevedo, J.L.F., Scalabrin, L.C. and Basso, E., 2013. "A study of physical and numerical effects of dissipation on turbulent flow simulations". *Journal of Aerospace Technology and Management*, Vol. 5, No. 2, pp. 145–168.

Kroll, N., Heinrich, R., Krueger, W. and Nagel, B., 2008. "Fluid-Structure Coupling for Aerodynamic Analysis and Design: A DLR Perspective - Invited". In *46th AIAA Aerospace Sciences Meeting and Exhibit*. Reno, Nevada.

MSC, 2004. *MSC Nastran 2004: Quick Reference Guide*.

Reimer, L., Braun, C., H Chen, B. and Ballmann, J., 2007. "Computational aeroelastic design and analysis of the hirenasd wind tunnel wing model and tests".

Rendall, T.C.S. and Allen, C.B., 2009. "Efficient mesh motion using radial basis functions with data reduction algorithms". *Journal of Computational Physics*, Vol. 228, No. 17, pp. 6231–6249.

Saad, Y., 2003. *Iterative Methods for Sparse Linear Systems*. Society for Industrial and Applied Mathematics, Philadelphia, PA, USA, 2nd edition.

8. RESPONSIBILITY NOTICE

The authors are solely responsible for the printed material included in this paper.